Approximating Periodic Potential Energy Surfaces with Sparse Trigonometric Interpolation

Zack Morrow,[†,¶] Chang Liu,[‡,¶] C. T. Kelley,[*,†] and Elena Jakubikova[*,‡]

[†]*Department of Mathematics, North Carolina State University, Raleigh, NC 27695*

[‡]*Department of Chemistry, North Carolina State University, Raleigh, NC 27695*

[¶]*Contributed equally to this work*

E-mail: tim_kelley@ncsu.edu; ejakubi@ncsu.edu

Abstract

The potential energy surface (PES) describes the energy of a chemical system as a function of its geometry and is a fundamental concept in computational chemistry. A PES provides much useful information about the system, including the structures and energies of various stationary points, such as local minima, maxima, and transition states. Construction of full-dimensional PESs for molecules with more than ten atoms is computationally expensive and often not feasible. Previous work in our group used sparse interpolation with polynomial basis functions to construct a surrogate reduced-dimensional PESs along chemically significant reaction coordinates, such as bond lengths, bond angles, and torsion angles. However, polynomial interpolation does not preserve the periodicity of the PES gradient with respect to angular components of geometry, such as torsion angles, which can lead to nonphysical phenomena. In this work, we construct a surrogate PES using trigonometric basis functions, for a system where the selected reaction coordinates all correspond to the torsion angles, resulting in a periodically repeating PES. We find that a trigonometric interpolation basis not only guarantees periodicity of the gradient, but also results in slightly lower approximation error than polynomial interpolation.

Introduction

The potential energy surface (PES) of an electronic state of a chemical system is a function that maps the molecular geometry to the electronic energy within the Born–Oppenheimer approximation.[1,2] Local structures of a PES, such as minima and saddle points, provide the geometry and energy information for stable and transition-state structures of a system. In addition, global features of PESs, which can be investigated by theoretical analyses[3,4] and via molecular-dynamics simulations,[5–10] are useful for understanding chemical reactivity. In order to construct a PES efficiently, different methods have been developed, such as modified Shepard interpolation,[11–13] permutationally invariant potential energy surface by linear least squares fitting,[5–7,14–16] neural network approaches,[17–19] Gaussian process,[20,21] and the finite-element method.[22–24] Most of these techniques focus on constructing a full-dimensional PES, which treats the potential energy of an N-atom system as a function of $3N - 6$ internal coordinates. Because the computational cost for constructing a PES increases rapidly with N, these full-dimensional methods are restricted to small molecules only (i.e., $N \leq 10$).

Fortunately, constructing a PES with all internal degrees of freedom (dofs) is not always necessary for studying the chemical reactivity of large systems with tens to hundreds of atoms. In many cases, only a small number of dofs, i.e., reaction coordinates (RCs), are essential for describing the system's chemical reactivity.[25] As a result, reduced-dimensional PESs with a small number of RCs have been widely employed to study various processes in large systems, such as the folding of polypeptides[26–28] and the intersystem crossing of transition-metal complexes.[4,29,30]

Previously,[10,31] we implemented the Smolyak sparse-grid interpolation algorithm[32,33] to build the reduced-dimensional PESs, where the interpolation basis functions are Lagrange polynomials with the Clenshaw–Curtis points.[34,35] This approach was shown to be efficient for both PES constructions and single-point energy evaluations.[10,31] In addition, we developed a new molecular dynamics (MD) simulation method for reduced-dimensional PESs.[9] The new MD method relies on interpolated potential energy and coordinate functions, and their derivatives (first-order for energy function and second-order for coordinate functions) to solve the classical equations of motion in the Hamiltonian formalism.[36,37] As a result, to generate smooth MD trajectories, the interpolated energy function must have continuous first derivatives, and the coordinate functions must have continuous second derivatives. These smoothness conditions apply to the whole domain, including the crossing of the periodic boundary.

The requirement for smoothness can be easily achieved within the domain for interpolation functions with polynomial basis. In one dimension, a polynomial of degree N on a closed interval $[a, b]$ is N times non-trivially continuously differentiable in the interior (a, b).

When RCs only contain non-periodic coordinates, such as bond lengths, bending angles and normal coordinates, the MD trajectories are constrained within the interpolation domain because of the high potential energy barrier at the boundary. In those cases, the polynomial basis is capable of providing the desired smoothness.

On the other hand, internal rotations often play important roles in monomolecular reactions, such as the photoisomerization of polymers and biomolecules,[38–40] hydrocarbon pericyclic reactions,[41] and spin crossover of transition metal complexes.[42,43] In many cases, one or more torsion angles are the primary reaction coordinates for describing the reaction process, while the remaining internal coordinates will only change slightly during the reaction to assist the primary reaction coordinates.[44–46] Reduced-dimensional PESs for these systems have an additional requirement for continuity: periodicity at boundaries. Polynomial interpolation will preserve periodicity of the underlying function values but gives no guarantees on the periodicity of the derivative. This causes the gradient of the surrogate PES to be discontinuous when an internal rotation crosses the periodic boundary. The left and right derivatives exist on either side, but they do not match. When a coordinate crosses the periodic boundary during an MD simulation, both kinetic energy and generalized forces will change suddenly with the discontinuous gradient,[9] leading to an incorrect MD result. Thus, an interpolation algorithm with other basis functions is necessary for modeling reactions with periodic coordinates.

In this work, we present a new sparse-grid interpolation method with a trigonometric basis.[34,47] Instead of constructing an interpolant with polynomial basis functions, we use sines and cosines, which guarantee periodicity of the surrogate PES gradient with respect to internal rotations. We employ the $[\mathrm{W(Cp)(CO)_3}]_2$ molecule as a model to test our new interpolation algorithm (see Figure 1). The energy barrier for gauche–anti interconversion of the molecule is 15.2 kcal/mol,[1] based on nuclear-resonance measurements.[48] Two-dimensional PESs were constructed with polynomial and trigonometric basis functions, where the RCs

---

[1] 1 kcal = 4.184 kJ.

correspond to the rotation of [W(Cp)(CO)$_3$] monomer (x_1) and the rotation of a Cp ring (x_2). A comparison of the two PESs is presented to show the advantages of a trigonometric basis for periodic coordinates.

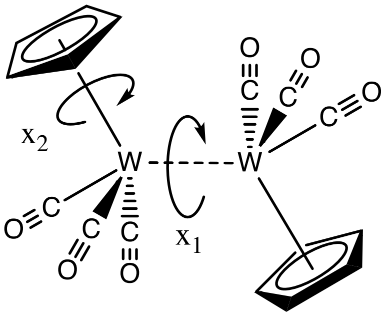

Figure 1: Model molecule used in this work, [W(Cp)(CO)$_3$]$_2$.

Computational Details

In this section, we describe how sparse grids can approximate a potential energy surface (PES) for a molecule. The full PES $\mathcal{E}_n(\boldsymbol{q})$ is a function of $\boldsymbol{q} \in \mathbb{R}^{3N-6}$ redundant geometry coordinates, where N is the number of atoms. We first partition $\boldsymbol{q} = (\boldsymbol{x}, \boldsymbol{\xi})$, where $\boldsymbol{x} \in \mathbb{R}^d$ are the design variables and $\boldsymbol{\xi}$ are remainder variables. Then we minimize over $\boldsymbol{\xi}$ to find the relaxed PES:

$$E_n(\boldsymbol{x}) = \min_{\boldsymbol{\xi}} \mathcal{E}_n(\boldsymbol{x}, \boldsymbol{\xi}) \tag{1}$$

A priori chemical considerations or knowledge of the system guides the selection of the design and remainder variables.

Equation (1) requires an optimization over $\boldsymbol{\xi}$, as well as solving (approximately) the Schrödinger equation for each $\boldsymbol{q} = (\boldsymbol{x}, \boldsymbol{\xi})$ in the optimization iteration. Due to the computational expense involved, directly evaluating (1) in a dynamical simulation is impractical for systems with $N > 10$, necessitating a surrogate model $E_n^s(\boldsymbol{x})$. Moreover, when E_n and ∇E_n are periodic, the surrogate model E_n^s and ∇E_n^s must also be periodic. Sparse polynomial interpolation can approximate a PES for dynamical simulations.[10] As noted previously in the literature,[10] sparse interpolation improves the ratio of approximation accuracy to the number of nodes, leading to a more efficient approximate PES with respect to the number of expensive ab initio calculations. When populating the nodes, each ab initio calculation is independent of the others, so the expensive part of the surrogate model is parallelizable. However, a polynomial interpolation basis can—and, in practice, does—fail to enforce periodicity of ∇E_n^s, leading to nonphysical dynamics. We now describe a sparse interpolation algorithm that uses a trigonometric interpolation basis, which enforces periodicity of ∇E_n^s.

Sparse trigonometric interpolation

The sparse trigonometric interpolant of $E_n(\boldsymbol{x})$ is

$$E_n^s(\boldsymbol{x}) = G_L^d[E_n](\boldsymbol{x}) = \sum_{\|\boldsymbol{i}\|_1 \leq L} (-1)^{L-\|\boldsymbol{i}\|_1} \binom{d-1}{L-\|\boldsymbol{i}\|_1} \mathcal{U}^{\boldsymbol{i}}[E_n](\boldsymbol{x}) \tag{2}$$

where G_L^d is the sparse trigonometric interpolation operator, $\boldsymbol{i} \in \mathbb{N}_0^d$ is a multi-index, and $\mathcal{U}^{\boldsymbol{i}}$ is a tensor-product interpolation operator.[34,47,49] The dimension is d, and L is the frequency of exactness, where we interpret frequency analogously to polynomial total degree. To construct the sparse interpolant, all we require is a set of model outputs $f_{\boldsymbol{j}}$ at the sparse-grid nodes $\boldsymbol{x}_{\boldsymbol{j}}$. Though this up-front cost of evaluating (1) at these nodes may be high, it is a one-time computation, and each evaluation of (2) is negligible in comparison.

While this may appear superficially similar to the algorithm in previous work on sparse polynomial interpolation,[10] our interpolation basis functions are tensor products of sines and cosines with different frequencies, rather than Lagrange polynomials. We use the TASMANIAN sparse-grid package in our computations.[34,50,51] The full mathematical details underlying (2) are in the Supporting Information for the interested reader. We now highlight five important details.

First, trigonometric interpolation is sensible only when E_n is periodic with respect to *every* component of $\boldsymbol{x}$. Otherwise, Gibbs effects will appear at the domain boundary for the nonperiodic component.[52] Continuity and piecewise differentiability are sufficient to ensure that trigonometric interpolation converges uniformly.[53] Higher orders of differentiability will increase the convergence rate.

Second, the choice of d and L uniquely determines the set of interpolation nodes $\mathcal{H}(d, L)$. Figure 2 shows two such set of nodes, $\mathcal{H}(2, 2)$ and $\mathcal{H}(2, 3)$. The canonical domain is $[0, 1]^d$, but we map the nodes into an interval $[a_i, b_i]$ that is suitable for the geometry coordinate x_i.[34] For instance, with the dihedral rotation of a hexagonal group, a suitable domain would be $[0°, 60°]$.

Third, the set of nodes is nested with respect to L. This is advantageous because if we decide to increase L to get more accuracy, we only need to evaluate Equation (1) for the *additional* nodes. Figure 2 displays the nestedness property.

Fourth, the number size of $\mathcal{H}(d, L)$ grows like $\mathcal{O}(d^L)$ for sufficiently large d.[47] This is in contrast with full-tensor interpolation having N nodes in each direction, which has N^d nodes in total. Even for moderate dimensions ($d \approx 5$), this cost reduction can be highly advantageous.

Fifth, we may want more points in certain dimensions than in others—for example, if a function is significantly less smooth along a particular dimension. In these cases, we replace $\|\boldsymbol{i}\|_1$ in Equation (2) with $\boldsymbol{i} \cdot \boldsymbol{\alpha}$, where $\boldsymbol{\alpha}$ is the anisotropy vector. See the Supporting Information for more details.

Electronic structure calculations

All electronic structure calculations were carried out in the Gaussian 16 software package[54] with the B3LYP functional.[55–58] The SDD pseudopotential and its associated basis set[59] were used for W, and the 3-21G basis set[60–65] was used for H, C, and O in all calculations. The 3-21G basis set was chosen to reduce the computational cost of PES construction and validation. The optimized geometry produced by this level of theory agrees well with the crystal structure[48] of the $[W(Cp)(CO)_3]_2$ molecule (see Supporting Information, Table S1).

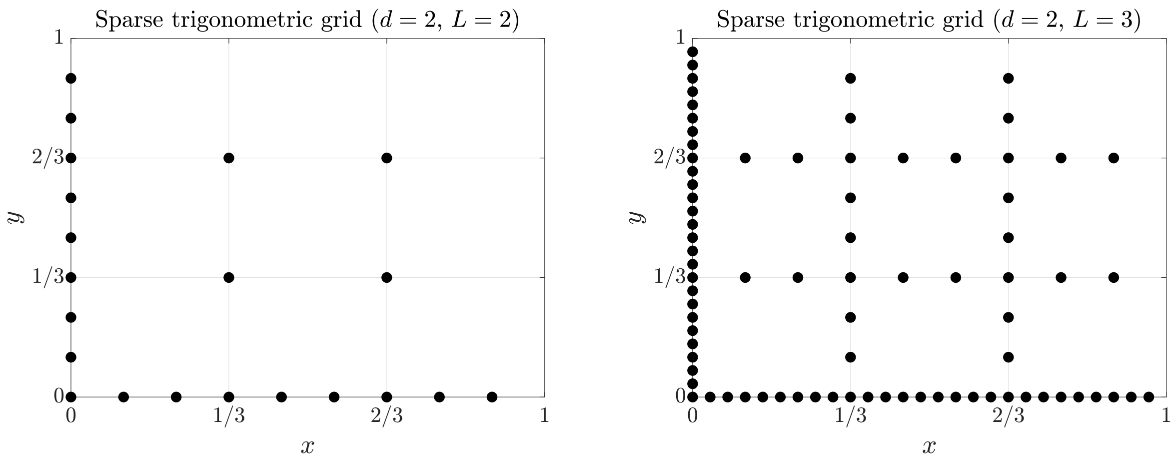

(a) (b)

Figure 2: Sparse trigonometric grids in $d = 2$ for (a) $L = 2$, (b) $L = 3$.

Previous computational studies with 3-21G basis set and B3LYP functional on transition metal complexes and organic molecules also showed their ability to reproduce optimized structures, frequencies and PESs with the accuracy comparable to calculations with larger basis sets.[66–69] Most importantly, the performance of the interpolation algorithm presented in this work is independent of the exact model chemistry utilized since the periodicity of the constructed PES and its gradient will not depend on the level of theory employed in the electronic structure calculations.

Frequency analysis was applied after each unconstrainted optimization to guarantee that a stationary point of the correct type was found. The geometry of the molecule is defined in Z-matrix format with four dummy atoms (see Figure 3 and Supporting Information Sec. 2). Two dihedral angles, X1–W1–W2–X3 (x_1) and C1–X1–W1–W2 (x_2), were employed as the design variables for the construction of the PES. The domains for interpolation are $[0, 360)$ for x_1 and $[0, 72)$ for x_2. The following symmetry was employed to further reduce the number of DFT calculations for the PES construction:

$$E(x_1, x_2) = E(360 - x_1, 72 - x_2)\,.$$

By exploiting this symmetry, we only need to run electronic structure calculations for nodes with $x_1 \in [0, 180]$ in order to populate the sparse-grid nodes.

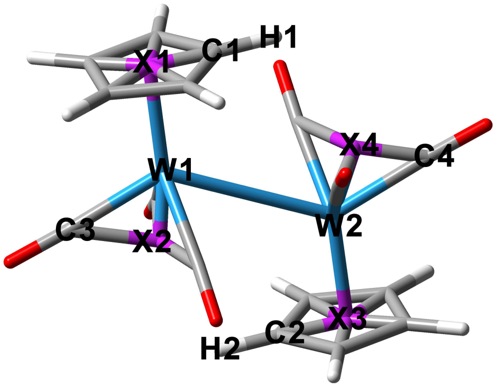

Figure 3: Global minimum structure for $[W(Cp)(CO)_3]_2$. Atoms X1–X4 are dummy atoms in the Z-matrix definition.

Results

We constructed two surrogate PESs for the ground state of the $[W(Cp)(CO)_3]_2$ molecule, shown in Figure 1 with the design variables x_1 and x_2 labeled. One PES employs the sparse polynomial interpolant used by Nance, Jakubikova, and Kelley.[10] The other utilizes the sparse trigonometric interpolant of $E_n(\boldsymbol{x})$, whose mathematical machinery is described in the "Approximation of potential energy surfaces" section. The second approach has not previously been deployed in surrogate PES modeling. We will test the following hypotheses: that a sparse trigonometric interpolant

(a) yields a more accurate approximation than a polynomial interpolation basis, and

(b) enforces periodicity of $\nabla E_n^s(\boldsymbol{x})$ to numerical accuracy.

Summary of main findings

Sparse grids for the trigonometric and polynomial interpolants are shown in Figure 4. Interpolation domains are $x_1 \in [0, 360]$ and $x_2 \in [0, 72]$ since x_2 corresponds to the rotation of a pentagonal group. The trigonometric grid has 135 points; the polynomial grid has 145 points. After evaluating the true PES $E_n(\boldsymbol{x})$ at each node shown in Figure 4, we invoked a simple call to TASMANIAN[34] to construct the surrogate potential energy surfaces shown in Figure 5. Apart from the nodes (shown as black dots), the surfaces in Figure 5 look similar to the eye along the x_1 direction. Furthermore, the shape of the PES and the different minimum-energy paths in Figure 5 suggest that the rotation of the Cp ring (x_2) is coupled with the rotation of the [W(Cp)(CO)$_3$] monomer (x_1). Non-differentiability of the true PES at the ridges along $x_1 = 120$ and $x_1 = 240$ slows the theoretical convergence rate of interpolation error but does not pose problems otherwise.[47]

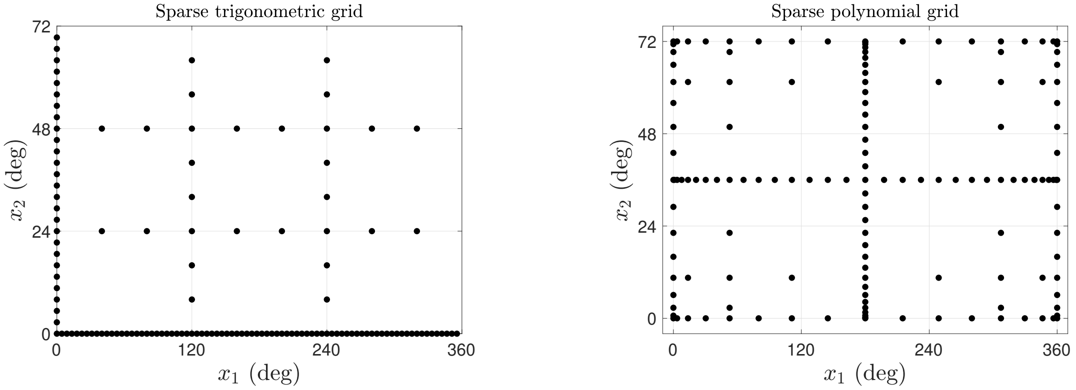

Figure 4: Left: Anisotropic sparse grid for trigonometric interpolant ($d = 2$, $L = 4$, $\boldsymbol{\alpha} = (5, 6)$). Note that we have more points along x_1 than x_2. Right: Sparse grid for polynomial interpolant using Clenshaw–Curtis nodes ($d = 2$, $L = 5$).

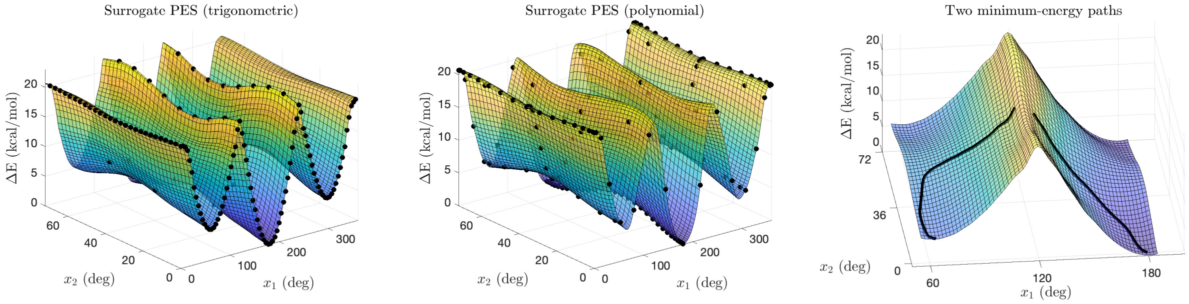

Figure 5: Surrogate ground state ($n = 0$) PES corresponding to the sparse grids in Figure 4. Interpolation nodes shown as black dots.

To quantify the error of our two surrogates versus the true PES, we randomly sampled 200 values of (x_1, x_2) from a uniform distribution on $[0, 360] \times [0, 72]$ using MATLAB's `rand` command, displayed in Figure 6. For each validation point, we performed a constrained optimization at the B3LYP/(SDD,3-21G) level of theory and compared the DFT-calculated energy to a single-point evaluation of the surrogate PES. We display the root-mean-square error (RMSE) and maximum absolute error (MAE) in Table 1. The 95% confidence interval for RMSE is calculated by treating the mean-squared error as a χ^2 random variable with 200 degrees of freedom.[70]

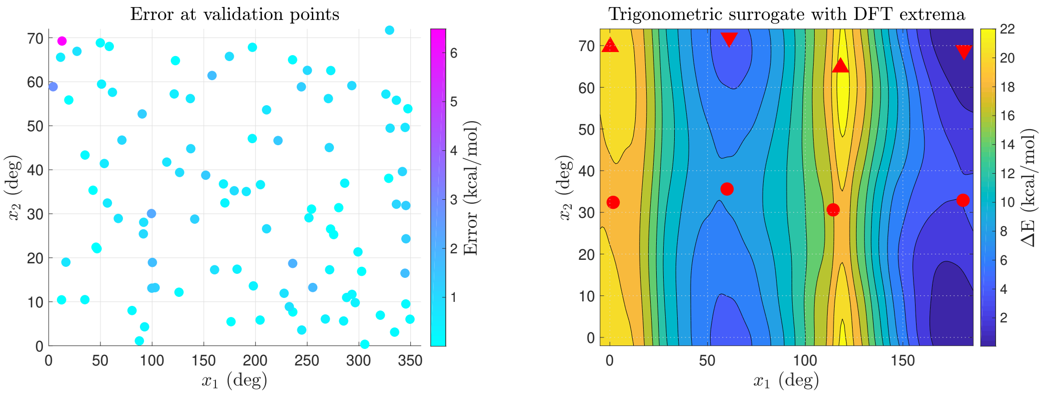

Figure 6: Left: 200 validation points. The points are colored based on the trigonometric surrogate PES error relative to the DFT-calculated energies. Right: Location of DFT extrema (minima are downward-pointing triangles, maxima are upward-pointing triangles, and saddle points are dots).

Table 1: Error against true values of PES at 200 points drawn from uniform distribution on $[0, 360] \times [0, 72]$. Units are kcal/mol.

	Trigonometric	Polynomial
RMSE	0.70	1.26
RMSE 95% conf. int.	$(0.63, 0.77)$	$(1.15, 1.40)$
MAE	2.15	4.14

In addition, we compared the energy and geometry of minima, maxima and saddle points on the two surrogate PESs with the fully optimized DFT structures. We display the DFT extrema on top of a contour plot of the trigonometric surrogate in Figure 6. As described in the methodology section, DFT-optimized structures are characterized by the number of imaginary frequencies (i.e., zero for minima, one for saddle points, and two for maxima on a two-dimensional PES). Details of the electronic structure calculations that produced these structures are described in Supporting Information Sec. 2. The optimized dihedral angles and relative energies for those stationary points are summarized in Table 2. The error from the trigonometric interpolant is smaller than the error of polynomial interpolant.

Table 2: Dihedral angles and relative energies of stationary points from PESs and DFT optimizations. The energy in the table is relative to the minimum-energy conformation with x_1 close to 180 degrees. Units of x_1 and x_2 are degrees; units of E_{rel} are kcal/mol.

Type	DFT			Trigonometric			Polynomial		
	x_1	x_2	E_{rel}	x_1	x_2	E_{rel}	x_1	x_2	E_{rel}
max	0.2	69.7	20.7	2.9	64.9	20.7	4.1	66.3	20.8
saddle	1.7	32.4	19.9	-2.0	35.5	19.9	-1.9	39.0	19.9
min	61.1	71.9	5.1	63.0	70.1	5.2	66.6	72.7	4.6
saddle	60.0	35.6	7.5	56.5	38.1	8.1	62.3	35.7	7.7
max	118.1	64.8	23.4	119.3	60.6	23.1	121.7	82.2	20.8
saddle	114.3	30.6	21.8	118.8	25.6	19.6	122.2	49.2	18.7
min	181.3	68.9	0.0	180.0	71.8	0.0	177.6	68.4	0.0
saddle	180.8	32.9	3.3	180.1	36.1	4.1	180.4	33.1	3.3
RMSE				2.7	3.6	0.9	4.4	9.4	1.4

Next, we examined the mismatch of the surrogate PES gradient. We compute the maximum x_1-gradient mismatch as

$$\max_{x_2 \in [0,72]} |f_{x_1}(0, x_2) - f_{x_1}(360, x_2)|$$

where $f_{x_1}(0, x_2)$ is understood to be a derivative from the right, and $f_{x_1}(360, x_2)$ is a derivative from the left. The maximum x_2-gradient mismatch is computed analogously. These results are shown in Table 3. The numerical error of forward and backward differences is $\mathcal{O}(h)$, where h is the step size. Therefore, since the maximum mismatches in the trigonometric case are indeed $\mathcal{O}(h)$, they are numerically zero. In contrast, the mismatches in the polynomial case are far larger than $\mathcal{O}(h)$.

Table 3: Gradient mismatches for trigonometric and Clenshaw–Curtis bases. Right/left derivatives approximated by forward/backward differences with step size $h = 10^{-5}$.

	Trigonometric	Polynomial
Max x_1-gradient mismatch	9.02×10^{-6}	2.05×10^{-1}
Max x_2-gradient mismatch	2.99×10^{-5}	9.62×10^{-1}

Discussion

The visual results in Figure 5 look reasonable for the two choices of surrogate. There are peaks when $x_1 = 120$ and $x_1 = 240$, and a global minimum occurs at $x_1 = 180$ as expected from empirical studies.[48] The real significance is in Tables 1 and 2, which demonstrate that the error for the trigonometric interpolant is smaller (by ∼0.5 kcal/mol on average) than the error for the polynomial interpolant. The maximum absolute error is almost exactly 2 kcal/mol smaller for the trigonometric interpolant. Recall that the trigonometric sparse grid has 135 nodes and the polynomial sparse grid has 145 nodes. Sparse trigonometric interpolation results in a more accurate surrogate PES than sparse polynomial interpolation at no increase in the number of evaluations of $E_n(\boldsymbol{x})$ (as measured by the number of nodes).

Additionally, the numerical results in Table 3 indicate that $\nabla E_n^s(\boldsymbol{x})$ is periodic when we use the trigonometric interpolation basis. The discretization error for forward/backward differences is $\mathcal{O}(h)$, which is precisely what we observe for the trigonometric basis. For the Clenshaw–Curtis polynomial basis, we observe a real-life example of ∇E_n^s failing to be periodic. Importantly, this failure occurs even though ∇E_n is periodic (since x_1 and x_2 are rotations). Thus, for applications where it is an absolute necessity that the surrogate PES gradient be periodic, a polynomial interpolant should *not* be used. Furthermore, the discussion in the previous paragraph indicates that, due to improved accuracy at no extra cost, one should consider using a trigonometric interpolation basis even when periodicity of the gradient is not a rigid requirement.

For each interpolation basis, we observed a significantly larger error for the two structures with x_1 close to 120 degrees. The larger errors occur because optimized geometries in this region mix two possible conformations: the locked conformation and the unlocked conformation (see Figure 7). When x_1 is smaller than 120 degrees, one CO group of one [W(Cp)(CO)$_3$] monomer is pointing at the center of two CO groups of the other monomer in the lowest energy conformations, because such conformations minimize the steric effect for conformations with small x_1 values. For the same reason, at large x_1 values, the unlocked conformation is more favorable than the locked conformation. As a result, the optimized geometries differ on opposite sides of 120 degrees. The cusp of the true PES makes this local region poorly described by the PES approximation with x_1 and x_2. Furthermore, due to the global definition of the interpolation basis functions, the quality of the entire surrogate is affected.

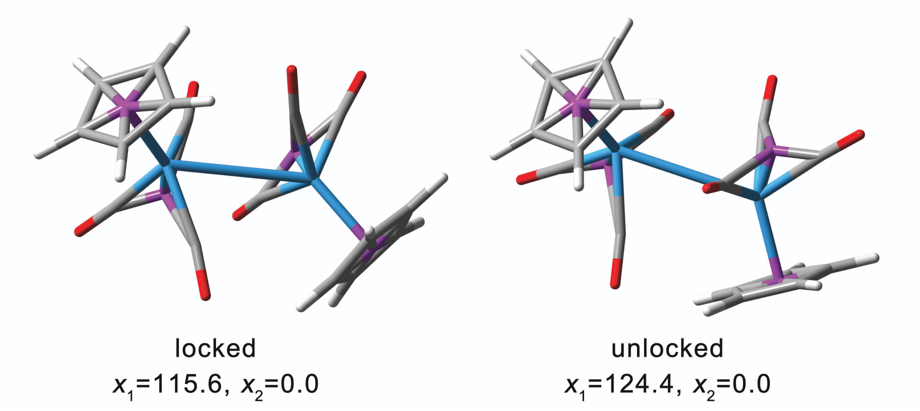

Figure 7: Locked and unlocked structures near $x_1 = 120$ and $x_2 = 0$.

As a caveat, the trigonometric interpolation algorithm we presented should only be used in problems where the PES is periodic in *all* components of $\boldsymbol{x}$ (i.e., all interesting geometry features are bond angles or dihedral angles). Approximating a non-periodic function with sines and cosines leads to poor accuracy at the edges of the domain, known as the Gibbs phenomenon.[52]

Conclusion

Periodic coordinates, such as internal rotations, often play important roles in chemical reactions. In order to construct a proper PES with those coordinates for MD simulations, the interpolation algorithm must provide continuous function values and gradients, both within the domain and crossing the boundaries. Conventional interpolation algorithms using polynomial basis functions do not guarantee the continuity of the gradient.

In this paper, we have presented a sparse interpolation algorithm that preserves the periodicity of the surrogate PES gradient. This algorithm uses sines and cosines as interpolation basis functions. We tested the interpolation algorithm by constructing a two-dimensional surface for a tungsten molecule, $[W(Cp)(CO)_3]_2$. Compared to sparse interpolation with a polynomial basis, the trigonometric basis we have employed provides smaller errors for both approximated energies and the stationary geometries from DFT calculations. Additionally, the framework of sparse interpolation improves the ratio of approximation accuracy to the number of nodes, leading to a more efficient approximate PES with respect to the number of expensive ab initio calculations.

To extend the applicability of this approach, we are currently investigating ways to construct a surrogate PES with both rotations and bond lengths as degrees of freedom. This algorithm would use polynomial basis functions on bond lengths and trigonometric basis functions on bond angles and dihedral angles.

Supporting Information

Mathematic details of sparse trigonometric interpolation, Gaussian 16 input, comparison of calculated and crystal structures (pdf). Data for trigonometric and polynomial PESs (xlsx).

Acknowledgement

We gratefully acknowledge support from the National Science Foundation under Grants No. OAC-1740309 and DMS-174564 (C.T.K.), CHE-1554855 (C.L. and E.J.), and an NSF Graduate Research Fellowship under DGE-1746939 (Z.M.). This work used the Extreme Science and Engineering Discovery Environment (XSEDE) Bridges at the Pittsburgh Supercomputing Center through Allocation No. TG-DMS180043 and the High-Performance Computing Center at NCSU. XSEDE is supported by NSF ACI-1548562.[71]

References

(1) Born, M.; Fock, V. Beweis des Adiabatensatzes. *Z. Phys.* **1928**, *51*, 165–180.

(2) Born, M.; Oppenheimer, R. Zur Quantentheorie der Molekeln. *Ann. Phys. – Berlin* **1927**, *389*, 457–484.

(3) Glasstone, S.; Eyring, H.; Laidler, K. J. *The Theory of Rate Processes*; McGraw-Hill, New York, 1941.

(4) Nance, J.; Bowman, D. N.; Mukherjee, S.; Kelley, C. T.; Jakubikova, E. Insights into the Spin-State Transitions in $[Fe(tpy)_2]_2{}^+$: Importance of the Terpyridine Rocking Motion. *Inorg. Chem.* **2015**, *54*, 11259–11268.

(5) Albaugh, A.; Boateng, H. A.; Bradshaw, R. T.; Demerdash, O. N.; Dziedzic, J.; Mao, Y.; Margul, D. T.; Swails, J.; Zeng, Q.; Case, D. A. et al. Advanced Potential Energy Surfaces for Molecular Simulation. *J. Phys. Chem. B* **2016**, *120*, 9811–9832.

(6) Bowman, J. M.; Czakó, G.; Fu, B. High-Dimensional Ab Initio Potential Energy Surfaces for Reaction Dynamics Calculations. *Phys. Chem. Chem. Phys.* **2011**, *13*, 8094–8111.

(7) Brown, A.; Braams, B. J.; Christoffel, K.; Jin, Z.; Bowman, J. M. Classical and Quasiclassical Spectral Analysis of CH_5^+ Using an Ab Initio Potential Energy Surface. *J. Chem. Phys.* **2003**, *119*, 8790–8793.

(8) Yagi, K.; Taketsugu, T.; Hirao, K. Generation of Full-Dimensional Potential Energy Surface of Intramolecular Hydrogen Atom Transfer in Malonaldehyde and Tunneling Dynamics. *J. Chem. Phys.* **2001**, *115*, 10647–10655.

(9) Liu, C.; Kelley, C. T.; Jakubikova, E. Molecular Dynamics Simulations on Relaxed Reduced-Dimensional Potential Energy Surfaces. *J. Phys. Chem. A* **2019**, 4543–4554.

(10) Nance, J.; Jakubikova, E.; Kelley, C. T. Reaction Path Following with Sparse Interpolation. *J. Chem. Theory Comput.* **2014**, *10*, 2942–2949.

(11) Collins, M. A. Molecular Potential-Energy Surfaces for Chemical Reaction Dynamics. *Theor. Chem. Acc.* **2002**, *108*, 313–324.

(12) Collins, M. A. Molecular Potential Energy Surfaces by Interpolation. *Lec. Notes Comput. Sc.* **2003**, 159–167.

(13) Collins, M. A.; Parsons, D. F. Implications of Rotation–Inversion–Permutation Invariance for Analytic Molecular Potential Energy Surfaces. *J. Chem. Phys.* **1993**, *99*, 6756–6772.

(14) Braams, B. J.; Bowman, J. M. Permutationally Invariant Potential Energy Surfaces in High Dimensionality. *Int. Rev. Phys. Chem.* **2009**, *28*, 577–606.

(15) Chen, Q.; Bowman, J. M. Quantum and Classical IR Spectra of $(HCOOH)_2$, $(DCOOH)_2$ and $(DCOOD)_2$ Using Ab Initio Potential Energy and Dipole Moment Surfaces. *Faraday Discuss.* **2018**, 33–49.

(16) Qu, C.; Yu, Q.; Bowman, J. M. Permutationally Invariant Potential Energy Surfaces. *Annu. Rev. Phys. Chem.* **2018**, *69*, 151–175.

(17) Jiang, B.; Li, J.; Guo, H. Potential Energy Surfaces from High Fidelity Fitting of Ab Initio Points: The Permutation Invariant Polynomial–Neural Network Approach. *Int. Rev. Phys. Chem.* **2016**, *35*, 479–506.

(18) Lorenz, S.; Groß, A.; Scheffler, M. Representing High-Dimensional Potential-Energy Surfaces for Reactions at Surfaces by Neural Networks. *Chem. Phys. Lett.* **2004**, *395*, 210–215.

(19) Manzhos, S.; Dawes, R.; Carrington, T. Neural Network-Based Approaches for Building High Dimensional and Quantum Dynamics-Friendly Potential Energy Surfaces. *Int. J. Quantum Chem.* **2014**, *115*, 1012–1020.

(20) Cui, J.; Krems, R. V. Gaussian Process Model for Collision Dynamics of Complex Molecules. *Phys. Rev. Lett.* **2015**, *115*, 073202.

(21) Uteva, E.; Graham, R. S.; Wilkinson, R. D.; Wheatley, R. J. Interpolation of Intermolecular Potentials Using Gaussian Processes. *J. Chem. Phys.* **2017**, *147*, 161706.

(22) Berweger, C. D.; van Gunsteren, W. F.; Müller-Plathe, F. Molecular Dynamics Simulation with an Ab Initio Potential Energy Function and Finite Element Interpolation: The Photoisomerization of cis-Stilbene in Solution. *J. Chem. Phys.* **1998**, *108*, 8773–8781.

(23) Berweger, C. D.; van Gunsteren, W. F.; Müller-Plathe, F. The Photoisomerization of cis-Stilbene Does Not Follow the Minimum Energy Path. *Angew. Chem. Int. Edit.* **1999**, *38*, 2609–2611.

(24) Berweger, C. D.; van Gunsteren, W. F.; Müller–Plathe, F. Finite Element Interpolation for Combined Classical/Quantum Mechanical Molecular Dynamics Simulations. *J. Comput. Chem.* **1998**, *18*, 1484–1495.

(25) Bolhuis, P. G.; Chandler, D.; Dellago, C.; Geissler, P. L. Transition Path Sampling: Throwing Ropes over Rough Mountain Passes, in the Dark. *Annu. Rev. Phys. Chem.* **2002**, *53*, 291–318.

(26) Dill, K. A.; Phillips, A. T.; Rosen, J. B. Protein Structure Prediction and Potential Energy Landscape Analysis Using Continuous Global Minimization. *P. Comput. Mol. Biol.* **1997**, 109–117.

(27) Komatsuzaki, T.; Hoshino, K.; Matsunaga, Y.; Rylance, G. J.; Johnston, R. L.; Wales, D. J. How Many Dimensions Are Required to Approximate the Potential Energy Landscape of a Model Protein? *J. Chem. Phys.* **2005**, *122*, 084714.

(28) Parchaňský, V.; Kapitán, J.; Kaminský, J.; Šebestík, J.; Bouř, P. Ramachandran Plot for Alanine Dipeptide as Determined from Raman Optical Activity. *J. Phys. Chem. Lett.* **2013**, *4*, 2763–2768.

(29) Boilleau, C.; Suaud, N.; Guihéry, N. Ab Initio Study of the Influence of Structural Parameters on the Potential Energy Surfaces of Spin-Crossover Fe(II) Model Compounds. *J. Chem. Phys.* **2012**, *137*, 224304.

(30) Sousa, C.; de Graaf, C.; Rudavskyi, A.; Broer, R.; Tatchen, J.; Etinski, M.; Marian, C. M. Ultrafast Deactivation Mechanism of the Excited Singlet in the Light-Induced Spin Crossover of $[\mathrm{Fe}(2,2'\text{-bipyridine})_3]_2{}^+$. *Chem. – Eur. J.* **2013**, *19*, 17541–51.

(31) Nance, J.; Kelley, C. T. A Sparse Interpolation Algorithm for Dynamical Simulations in Computational Chemistry. *SIAM J. Sci. Comput.* **2015**, *37*, S137–S156.

(32) Judd, K. L.; Maliar, L.; Maliar, S.; Valero, R. Smolyak Method for Solving Dynamic Economic Models: Lagrange Interpolation, Anisotropic Grid and Adaptive Domain. *J. Econ. Dyn. Control* **2014**, *44*, 92–123.

(33) Smolyak, S. A. Quadrature and Interpolation Formulas for Tensor Products of Certain Classes of Functions. *Dokl. Akad. Nauk.* **1963**, *148*, 1042–1045.

(34) Stoyanov, M. TASMANIAN Sparse Grids (version 6.0). Oak Ridge National Laboratory, Oak Ridge, TN, 2019; `https://tasmanian.ornl.gov`.

(35) Clenshaw, C. W.; Curtis, A. R. A Method for Numerical Integration on an Automatic Computer. *Numer. Math.* **1960**, *2*, 197–205.

(36) Deriglazov, A. *Classical Mechanics*; Springer-Verlag, Berlin, 2016.

(37) Lanczos, C. *The Variational Principles of Mechanics*; Courier Corporation, 2012.

(38) Liu, R. S. H.; Hammond, G. S. Examples of Hula-Twist in Photochemical cis–trans Isomerization. *Chem. – Eur. J.* **2001**, *7*, 4536–4545.

(39) Liu, R. S.; Asato, A. E. The Primary Process of Vision and the Structure of Bathorhodopsin: A Mechanism for Photoisomerization of Polyenes. *P. Natl. Acad. Sci. USA* **1985**, *82*, 259–263.

(40) Yamabe, T.; Akagi, K.; Ohzeki, K.; Fukui, K.; Shirakawa, H. Isomerization Mechanisms from cis to trans Form in Polyacetylene. *J. Phys. Chem. Solids* **1982**, *43*, 577–581.

(41) Houk, K. N.; Li, Y.; Evanseck, J. D. Transition Structures of Hydrocarbon Pericyclic Reactions. *Angew. Chem. Int. Edit.* **1992**, *31*, 682–708.

(42) Ashley, D. C.; Jakubikova, E. Ray-Dutt and Bailar Twists in Fe(II)-Tris(2,2'-bipyridine): Spin States, Sterics, and Fe–N Bond Strengths. *Inorg. Chem.* **2018**, *57*, 5585–5596.

(43) Purcell, K. F. Pseudorotational Intersystem Crossing in d^6 Complexes. *J. Am. Chem. Soc.* **1979**, *101*, 5147–5152.

(44) Li, W.; Ma, A. Reaction Mechanism and Reaction Coordinates from the Viewpoint of Energy Flow. *J. Chem. Phys.* **2016**, *144*, 114103.

(45) Tavadze, P.; Avendaño Franco, G.; Ren, P.; Wen, X.; Li, Y.; Lewis, J. P. A Machine-Driven Hunt for Global Reaction Coordinates of Azobenzene Photoisomerization. *J. Am. Chem. Soc.* **2018**, *140*, 285–290.

(46) Wiedbrauk, S.; Maerz, B.; Samoylova, E.; Reiner, A.; Trommer, F.; Mayer, P.; Zinth, W.; Dube, H. Twisted Hemithioindigo Photoswitches: Solvent Polarity Determines the Type of Light-Induced Rotations. *J. Am. Chem. Soc.* **2016**, *138*, 12219–12227.

(47) Hallatschek, K. Fouriertransformation auf Dünnen Gittern mit Hierarchischen Basen. *Numer. Math.* **1992**, *63*, 83–97.

(48) Adams, R. D.; Collins, D. M.; Cotton, F. A. Molecular Structures and Barriers to Internal Rotation in Bis(η^5-cyclopentadienyl)hexacarbonylditungsten and Its Molybdenum Analog. *Inorg. Chem.* **1974**, *13*, 1086–1090.

(49) Griebel, M.; Hamaekers, J. In *Sparse Grids and Applications – Munich 2012*; Garcke, J., Pflüger, D., Eds.; Lecture Notes in Computational Science and Engineering; Springer International Publishing Switzerland, 2014; Chapter 4, pp 75–107.

(50) Stoyanov, M. *Hierarchy-Direction Selective Approach for Locally Adaptive Sparse Grids*; 2013.

(51) Stoyanov, M. K.; Webster, C. G. A Dynamically Adaptive Sparse Grids Method for Quasi-Optimal Interpolation of Multidimensional Functions. *Comput. Math. Appl.* **2016**, *71*, 2449–2465.

(52) Helmberg, G. The Gibbs Phenomenon for Fourier Interpolation. *J. Approx. Theory* **1994**, *78*, 41–63.

(53) Morrow, Z.; Stoyanov, M. A Method for Dimensionally Adaptive Sparse Trigonometric Interpolation of Periodic Functions. 2019, arXiv:1908.10672. arXiv.org e-Print archive. `https://arxiv.org/abs/1908.10672` (accessed Sep. 27, 2019).

(54) Frisch, M. J.; Trucks, G. W.; Schlegel, H. B.; Scuseria, G. E.; Robb, M. A.; Cheeseman, J. R.; Scalmani, G.; Barone, V.; Petersson, G. A.; Nakatsuji, H. et al. Gaussian 16 Revision A.03. 2016; Gaussian Inc. Wallingford CT.

(55) Becke, A. D. Density-Functional Thermochemistry. III. The Role of Exact Exchange. *J. Chem. Phys.* **1993**, *98*, 5648–5652.

(56) Becke, A. D. A New Mixing of Hartree-Fock and Local Density-Functional Theories. *J. Chem. Phys.* **1993**, *98*, 1372–1377.

(57) Lee, C.; Yang, W.; Parr, R. G. Development of the Colle-Salvetti Correlation-Energy Formula into a Functional of the Electron Density. *Phys. Rev. B* **1988**, *37*, 785–789.

(58) Stephens, P. J.; Devlin, F. J.; Chabalowski, C. F.; Frisch, M. J. Ab Initio Calculation of Vibrational Absorption and Circular Dichroism Spectra Using Density Functional Force Fields. *J. Phys. Chem.* **1994**, *98*, 11623–11627.

(59) Kaupp, M.; Schleyer, P. v. R.; Stoll, H.; Preuss, H. Pseudopotential Approaches to Ca, Sr, and Ba Hydrides. Why Are Some Alkaline Earth MX_2 Compounds Bent? *J. Chem. Phys.* **1991**, *94*, 1360–1366.

(60) Binkley, J. S.; Pople, J. A.; Hehre, W. J. Self-Consistent Molecular Orbital Methods. 21. Small Split-Valence Basis Sets for First-Row Elements. *J. Am. Chem. Soc.* **1980**, *102*, 939–947.

(61) Dobbs, K. D.; Hehre, W. J. Molecular Orbital Theory of the Properties of Inorganic and Organometallic Compounds. 4. Extended Basis Sets for Third-Row and Fourth-Row, Main-Group Elements. *J. Comput. Chem.* **1986**, *7*, 359–378.

(62) Dobbs, K. D.; Hehre, W. J. Molecular Orbital Theory of the Properties of Inorganic and Organometallic Compounds. 5. Extended Basis Sets for First-Row Transition Metals. *J. Comput. Chem.* **1987**, *8*, 861–879.

(63) Dobbs, K. D.; Hehre, W. J. Molecular Orbital Theory of the Properties of Inorganic and Organometallic Compounds. 6. Extended Basis Sets for Second-Row Transition Metals. *J. Comput. Chem.* **1987**, *8*, 880–893.

(64) Gordon, M. S.; Binkley, J. S.; Pople, J. A.; Pietro, W. J.; Hehre, W. J. Self-Consistent Molecular-Orbital Methods. 22. Small Split-Valence Basis Sets for Second-Row Elements. *J. Am. Chem. Soc.* **1982**, *104*, 2797–2803.

(65) Pietro, W. J.; Francl, M. M.; Hehre, W. J.; DeFrees, D. J.; Pople, J. A.; Binkley, J. S. Self-Consistent Molecular Orbital Methods. 24. Supplemented Small Split-Valence Basis Sets for Second-Row Elements. *J. Am. Chem. Soc.* **1982**, *104*, 5039–5048.

(66) Estiú, G.; Rama, J.; Pereira, A.; Cachau, R. E.; Ventura, O. N. A Theoretical Study of Excited State Proton Transfer in 3-hydroxychromone and Related Molecules. *J. Mol. Struc. Theochem* **1999**, *487*, 221–230.

(67) Kukovec, B.-M.; Kodrin, I.; Mihalić, Z.; Furić, K.; Popović, Z. Cis–trans Isomerism in Cobalt(II) Complexes with 3-hydroxypicolinic Acid. Structural, DFT and Thermal Studies. *Inorg. Chim. Acta* **2010**, *363*, 1887–1896.

(68) Versiani Cabral, O.; Téllez S, C. A.; Giannerini, T.; Felcman, J. Fourier-Transform Infrared Spectrum of Aspartate Hydroxo-aqua Nickel (II) Complex and DFT-B3LYP/3-21G and 6-311G Structural and Vibrational Calculations. *Spectrochim. Acta A* **2005**, *61*, 337–345.

(69) Zandler, M. E.; D'Souza, F. The Remarkable Ability of B3LYP/3-21G(*) Calculations to Describe Geometry, Spectral and Electrochemical Properties of Molecular and Supramolecular Porphyrin–Fullerene Conjugates. *C. R. Chim.* **2006**, *9*, 960–981.

(70) Faber, N. M. Estimating the Uncertainty in Estimates of Root Mean Square error of Prediction: Application to Determining the Size of an Adequate Test Set in Multivariate Calibration. *Chemometr. Intell. Lab.* **1999**, *49*, 79 – 89.

(71) Towns, J.; Cockerill, T.; Dahan, M.; Foster, I.; Gaither, K.; Grimshaw, A.; Hazlewood, V.; Lathrop, S.; Lifka, D.; Peterson, G. D. et al. XSEDE: Accelerating Scientific Discovery. *Comput. Sci. Eng.* **2014**, *16*, 62–74.

TOC Graphic